The Swiss Light Source Upgrade to a Diffraction-Limited Storage Ring

Philip R. Willmott,* Gabriel Aeppli, Alun Ashton, Christoph Bostedt, Oliver Bunk, Marco Calvi, Yasin Ekinci, Uwe Flechsig, Romain Ganter, Terence Garvey, Markus Jörg, David Just, Roland Kobler, Frithjof Nolting, Luc Patthey, Claude Pradervand, Jörg Raabe, Leonid Rivkin, Benedikt Rösner, Thomas Schmidt, Andreas Streun, Friso van der Veen, and Hans Braun
Paul Scherrer Institute, CH-5232 Villigen, Switzerland
(Dated: February 24, 2022)

The Swiss Light Source (SLS) has been operational since 2001. In the last two decades, unique and world-leading scientific programs and methods have developed from the SLS in fields as diverse as macromolecular biology, imaging, and the electronic structure and behaviour of novel and complex materials. These achievements have been largely underpinned by the excellent performance of the electron accelerator and storage ring, which was considered the benchmark in this field until well into the second decade of this century. With the advent of novel technologies in accelerator physics and the consequent emergence of the next generation of storage-ring facilities, known as diffraction-limited storage rings (or DLSRs), it has now become imperative to upgrade the SLS in like manner. The general features of DLSRs, the characteristics of the new SLS 2.0 machine, and the scientific opportunities it will offer are the subject of this in-part didactic article.

Keywords: diffraction-limited storage ring, DLSR, synchrotron, x-rays, SLS, Swiss Light Source

I. INTRODUCTION

The Swiss Light Source (SLS) has been serving the international scientific community since 2001 in scientific endeavours as diverse as bioimaging, molecular biology, novel electronic materials, nanomagnetism, catalysis and energy research, and cultural heritage, to name just some examples. Indeed, two recent Nobel prizes were awarded for discoveries enabled by experimental data obtained at the SLS [1–4].

The SLS has been a highly attractive research tool for many reasons, including the reliability and stability of the performance of the storage ring. A decade after its inauguration, the horizontal electron emittance value of 5.5 nm rad (the concept of emittance is described below) was considered to be a benchmark for storage-ring facilities regarding how closely the actual performance approximated the theoretically minimum achievable value, given the ring size, storage-ring energy, and contemporary magnet-lattice technology [1].

Nonetheless, a quantum leap in storage-ring performance was promised by innovations in magnet fabrication and vacuum technologies that emerged in the first decade of this century [7]. To appreciate the approximately two orders of magnitude improvement in performance promised by these developments, the concept of the figure-of-merit for synchrotrons called the 'brightness', or 'brilliance', must be understood. We thus begin with a short exposition on machine physics.

II. SOME BASIC STORAGE-RING MACHINE PHYSICS

A. Brightness and emittance

Brightness encapsulates the most important parameters of synchrotron radiation in a single number (see Figure 1). It is defined as the flux of photons produced per unit time and in a defined bandwidth from a source exhibiting a certain source area and divergence, and is specifically given by

$$\mathcal{B} = \frac{\mathrm{ph/s}}{\sigma_x \sigma_y \times \sigma'_x \sigma'_y \times 0.1\%\,\mathrm{BW}}, \tag{1}$$

whereby $\sigma_{x,y}$ (in mm) and $\sigma'_{x,y}$ (in mrad) represent the source size and divergence, respectively, in the x- and y-directions. An undulator source at a modern third-generation synchrotron facility can expect to deliver brilliances of the order of 10^{19} to 10^{20} ph/(s $\cdot$ mm^2 $\cdot$ mrad^2 $\cdot$ 0.1% BW).

The combined quantity of source size and divergence found in the denominator of the expression for brilliance is referred to as emittance, ε. The horizontal emittance in the orbital plane, $\varepsilon_x = \sigma_x \sigma'_x$ is generally larger than the vertical emittance in the vertical plane $\varepsilon_y = \sigma_y \sigma'_y$.[2]

* Correspondence email address: philip.willmott@psi.ch

[1] The original SLS design was in fact what today is called a multi-bend achromat lattice. This design was attempted between 1993 and 1996 [5, 6]. The final design was changed to the present triple-bend achromat, as no suitable multi-bend solution could be found at the time.

[2] Here we neglect possible correlations between particle positions and angles. More precisely, emittance is defined as $\varepsilon_x = \sqrt{\langle x^2 \rangle \langle x'^2 \rangle - \langle x x' \rangle^2}$, with the brackets defining averages.

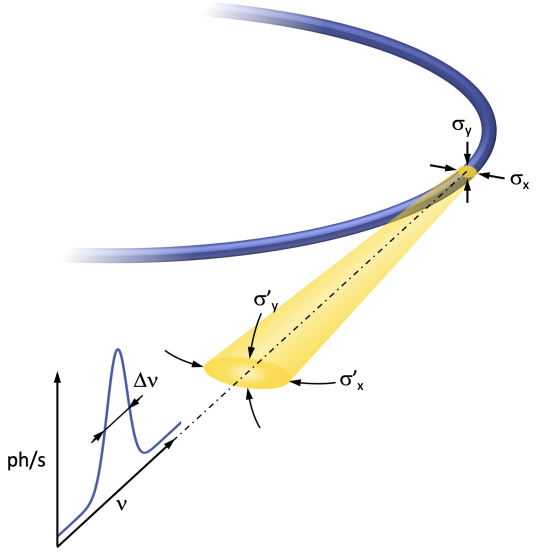

Figure 1. Schematic of the parameters determining brilliance, see Equation 1. The root-mean-square (RMS) source sizes ($\sigma_{x,y}$) and divergences ($\sigma'_{x,y}$) in the planes perpendicular to the direction of radiation define the emittance; the relative bandwidth is given by the bandwidth $\Delta\nu$ divided by the central frequency ν,[a] delivering a flux given in ph s^{-1}.

[a] The relationship between photon energy, wavelength, and frequency is $E = h\nu = hc/\lambda$.

Importantly, the emittance in any one plane is the convolution of the emittance associated with the electron beam, ε^e, with that due to photon emission, ε^p. The former is dictated by the details of the magnet lattice (more on which we discuss presently), while the latter is a fundamental property associated with diffraction phenomena and depends only on the photon wavelength. It can be shown that the source size and divergence of radiation from an undulator source of length L, ignoring contributions from the electron beam, are given by

$$\sigma^p = \sqrt{\lambda L}/4\pi; \tag{2}$$

$$\sigma'^p = \sqrt{\lambda/L}, \tag{3}$$

and hence

$$\varepsilon^p = \frac{\lambda}{4\pi}. \tag{4}$$

The ratio σ^p/σ'^p is referred to as the photonic beta function $\beta^p = L/4\pi$, which has units of length and is independent of the radiation wavelength. Analogously, the beta function of the electron beam is given by $\beta^e = \sigma^e/\sigma'^e$, which can be manipulated using electron optics.

In the hard x-ray regime for which $\lambda \sim 1$ Å (12-keV photons), the photon emittance is of the order of 10 pm rad. Even for photon energies in the regime of 1 keV, $\varepsilon^p \sim 100$ pm rad, the photon emittance is between one and two orders of magnitude smaller than the electron emittance in third-generation facilities.

B. Multibend achromats and the diffraction limit

The electron emittance is determined by the so-called radiation equilibrium: like in a spectrometer, the bending magnets forming the storage ring lattice deflect particles depending on their energy spread – an effect called dispersion. The quantum nature of photon emission introduces a stochastic spread of individual electron energies, which then is translated into the orbital plane through dispersion. On the other hand, continuous energy loss to radiation in combination with acceleration of the electrons in the radio frequency cavities of the storage ring provides damping of the energy fluctuations. Finally, the emittance of the electron beam is given by the competing effects of radiation damping and quantum excitation forming an equilibrium, which is solely determined by the structure of the magnet lattice.

Obviously, in order to adjust the equilibrium beam emittance to low values requires that the dispersion remains small inside the bending magnets. This means one should rather use many small bending magnets instead of a few big ones, in order to prevent the dispersion from growing to large values inside the magnet.

Thus, the quintessential feature of the fourth-generation synchrotron facility is the employment of so-called multibend achromats (MBAs) in the arc sectors of the storage ring. What is meant by this term? Classically, the arc sectors of synchrotrons, that is, the regions which are responsible for bending the electron beam into a closed path, are served by so-called double-bend achromats[3].

[3] Some third-generation facilities, notably the SLS, use a *triple* bend achromat, but this is a detail that need not concern us here.

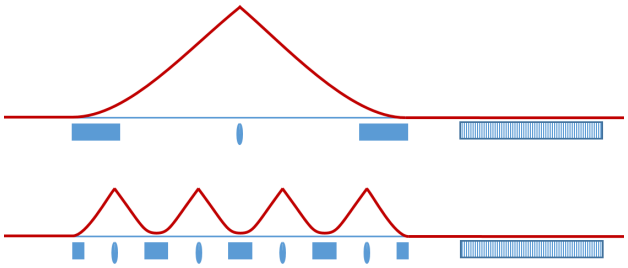

Figure 2. Schematics of a double bend achromat (DBA) and multi-bend achromat (MBA). The red line indicates the dispersion, which is refocused by magnetic lenses (quadrupoles) in order to minimize it inside the dipoles and to suppress it in the straight sections, where the undulators are located.

A double-bend achromat (DBA), as depicted in Figure 2, uses two bending-magnet dipoles separated by focusing quadrupole magnets. This is the most simple system to suppress dispersion in the straight sections. A multibend achromat is similar, but uses several small DBAs in a row, typically between 5 and 9, to execute a given arc angle. An MBA with M dipoles contains $(M-1)$ DBA cells (Figure 2 bottom).

Limiting the dispersion growth inside the bending magnets enables dramatic emittance reduction: calculating the *minimum* horizontal electron emittance theoretically attainable by an MBA structure we find that it is proportional to the third power of the bending angle θ of the dipole [8]. Precisely,

$$\varepsilon_x^e = \frac{C_q \gamma^2}{12\sqrt{15}\, J_x}\theta^3, \tag{5}$$

where $\gamma = \mathcal{E}/m_e c^2$ is the ratio of the storage ring energy to the electron rest-mass energy, and $C_q = 3.832 \times 10^{-13}$ m. The parameter J_x in the denominator depends on the distribution of radiation damping to transverse and longitudinal dimensions and typically has values between 1 and 2.

Note that ε_x^e depends on the square of the storage-ring energy. Despite this, the upgrade of the SLS includes an *increase* in this parameter from $\mathcal{E} = 2.4$ to 2.7 GeV, as this will facilitate access to photon energies well in excess of 40 keV, which is especially interesting for both imaging and chemical spectroscopies, two areas of research in which the SLS has historically been a leading player.

The path to low emittance by building a lattice from many small magnets became viable once miniaturization of accelerator components became feasible, in particular with regards to the magnets and the cross-section of the vacuum vessels containing the circulating electrons.

For a storage ring containing N arcs of M dipoles each, the bending angle per dipole simply is $\theta = 2\pi/N(M-1)$, and Equation 5 becomes

$$\varepsilon_x^e = \frac{2C_q\gamma^2\pi^3}{3\sqrt{15}\, J_x}\frac{1}{N^3(M-1)^3} \tag{6}$$

$$\Rightarrow \varepsilon_x^e[\mathrm{nm\,rad}] = 7834\frac{(\mathcal{E}\,[\mathrm{GeV}])^2}{J_x}\frac{1}{N^3(M-1)^3}. \tag{7}$$

Therefore, SLS 2.0, for which $N = 12$ and $M = 7$, has a theoretical ultimate horizontal electron emittance of 153 pm rad (for $J_x = 1$). The actual goal value, considering subtleties that go well beyond the scope of this introductory text, is $\varepsilon_x^e = 158$ pm rad (Figure 3).

From our expression given in Equation 4, we can calculate that radiation with the same emittance ε^p as ε_x^e will, for SLS 2.0, have a wavelength of 19.73 Å, equating to a photon energy of approximately 630 eV; these are referred to as the 'diffraction-limited wavelength' λ_{DL} and 'diffraction-limited energy' $h\nu_{\mathrm{DL}}$, respectively. For photon energies much smaller than this, the photon contribution to the total emittance dominates, and no substantial gain is made by attempts to improve the electron emittance further[4]. This is the meaning of diffraction-limited storage rings – their performance

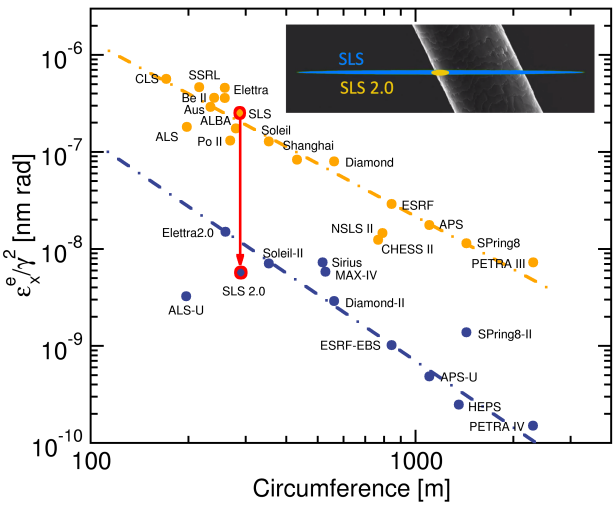

Figure 3. Plot of horizontal electron emittances weighted by the square of the storage-ring energy as a function of ring circumference (see Equation 5), for both a selection of third- (orange data points) and fourth-generation (blue) synchrotrons. Note the approximately fortyfold improvement in the weighted emittance for the SLS 2.0 upgrade, highlighted in red. The inset shows the cross-sections of the electron beams at SLS and SLS 2.0 compared to a typical human hair.

[4] Note that, for third-generation facilities, the 'diffraction-limited photon energy' is of the order of 20 eV.

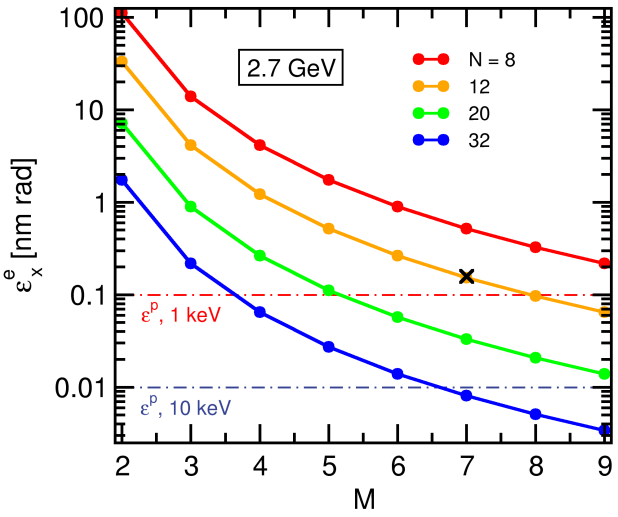

Figure 4. Plot of the theoretically optimal horizontal electron emittance ε_x^e as a function of the number of straights N in a 2.7-GeV synchrotron ring and number of dipoles M within a single arc sector, according to Equation 6. Values for $N = 12$, 20, and 32 were selected, as these correspond to SLS 2.0, MAX-IV, and ESRF-EBS, respectively. Also included as dot-dash lines are the fundamental photon emittances for 1 and 10-keV photons, given by Equation 4, and the position of SLS 2.0, labelled as the black X.

is limited, at least for photon energies below that for which $\varepsilon^p = \varepsilon_x^e$, by fundamental diffraction phenomena. We summarize this in Figure 4.

The electron emittance is a constant around the storage ring for a given magnet lattice. In the above, however, we have not considered how this is distributed between divergence and electron-beam size – is the beam very small but highly divergent (low β^e), or larger and more parallel (high β^e)? Importantly, although the electron emittance remains constant for a given ring, one can manipulate β^e using the electron optics such as the quadrupole magnets and the combined function magnets, which are magnets providing focusing and bending simultaneously. Now, because the total emittance is the convolution of the electron- and photon contributions, it is easy to demonstrate that the beta function of the electron emittance is optimized, and thereby the total emittance is minimized, when it equals that of the photon emittance, i.e., $L/4\pi$, that is, of the order of a few tens of cm, depending on the undulator length.

C. Coherence

To conclude this whistle-stop précis of the most important aspects of storage-ring and radiation parameters, we briefly discuss coherence. Within the figure of merit of brightness are the parameters that quantitatively define coherence – the emittance and the relative spectral bandwidth. Consider a broadband and spatially distributed source such as an incandescent light bulb (Figure 5). The source emittance can be reduced by placing a slit or pinhole in front of the source. This determines the 'spatial', or 'transverse' coherence. In the case of synchrotrons, the slit (or source) size is given by the transverse spatial extent of the beam. Even for soft x-ray sources below a few keV, this is dominated by the size of the electron beam, as this will be of the order of tens of microns or more, much larger than the radiation's wavelength, measured in nanometers or angstroms. The divergence is given by the Fourier transform of the source profile; accordingly, the full-width half-maximum (FWHM) subtended angle is approximately equal to the ratio of the wavelength to the beam FWHM, of the order of 10^{-4} rad for soft x-radiation. Secondly, a dispersive element such as a monochromator suppresses all radiation apart from a narrow bandwidth. Now, the radiation is both spatially and longitudinally (or temporally) coherent. Both the emittance and relative spectral bandwidth are included in the definition of brilliance.

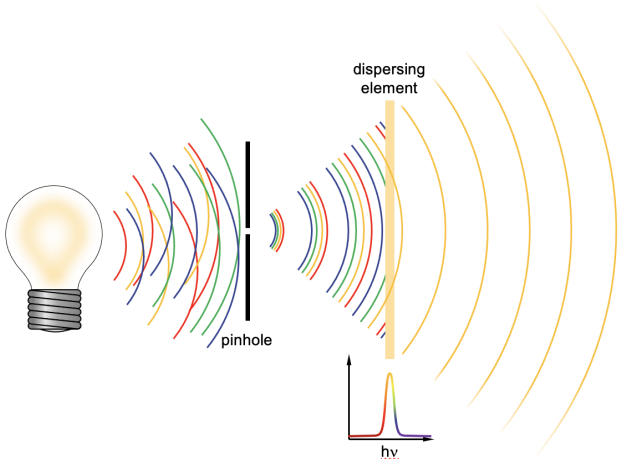

Figure 5. Coherent radiation can be extracted from a broadband, spatially extended source by the use of a pinhole and a dispersive element that selects a narrow band of wavelengths.

The transverse coherence length at a distance R from a source of width D is given by

$$l_c^{(t)} = \frac{\lambda R}{2D} = \frac{\lambda R}{2\sqrt{\pi}\sigma_{x,y}}. \tag{8}$$

Hence, in the orbital plane of the synchrotron, DLSRs have transverse coherence lengths of several hundred microns, up to two orders of magnitude larger than those typically found at third-generation facilities.

The 'temporal', or 'longitudinal' coherence length, determined by the degree of monochromacity, is given

by

$$l_c^{(l)} = \frac{\lambda^2}{\Delta\lambda}. \tag{9}$$

The temporal coherence length thus depends on any dispersive element in the beamline, particularly monochromators. A Si(111) double-crystal monochromator has an intrinsic relative bandwidth of approximately 1.4×10^{-4}, which, for 1-Å-radiation leads to $l_c^{(l)} \sim 1$ μm. Note that DLSR technologies do not intrinsically provide advantages in longitudinal coherence compared to third-generation facilities.

Finally, it should be noted that this definition of coherence is more relaxed in one aspect than that defining coherence in lasers and XFELs, namely in the phase relationship between individual emitters. The action of stimulated emission in a laser medium means that the stimulat*ed* radiation not only has the same photon energy and direction, but is also in phase with the stimulat*ing* radiation. The same is true for the self-amplified spontaneous emission (SASE) radiation pulses generated in XFELs – the electrons are bathed in the field of the radiation they produce and are squeezed into microbunches separated from one another by the radiation's wavelength. Hence, in the case of lasers and XFELs, the amplitudes of the N_p individual emitters add coherently and the intensity is therefore proportional to N_p^2. In the case of synchrotrons, emission is entirely stochastic and the coherent intensity is thus directly proportional to N_p.

III. SOURCES AT THE SLS 2.0 UPGRADE

A graphical summary of the expected brilliances of the x-ray sources at SLS 2.0 is provided in Figure 6 The six hard x-ray undulator beamlines are served by the CPMUs and one HTSU10, while four hard x-ray bending-magnet beamlines have two warm superbends (2.1 T) and two superconducting superbends (5 T). The five remaining straights produce soft and tender x-rays, and are served by combinations of the elliptical undulators (UEXX).

A. Hard x-ray undulators

An exciting aspect of the upgrade is that improvements in the brilliance also enable other innovations further down the technological chain, notably in the field of undulator development.

The description of the interference phenomena that lead to the spectral output from undulators is given by

$$m\lambda_m(\theta) = \frac{\lambda_u}{2\gamma^2}\left(1 + \frac{K^2}{2} + \gamma^2\theta^2\right), \tag{10}$$

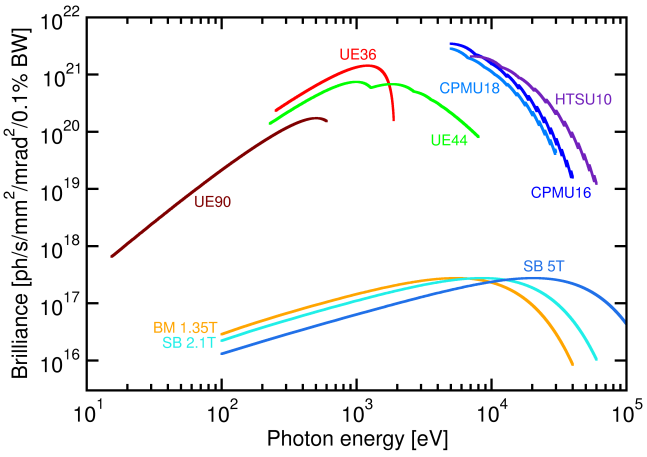

Figure 6. Brilliance curves of the SLS 2.0 sources. CPMU = cryogenic permanent-magnet undulator; HTSU = high-temperature superconducting undulator; UE = elliptical undulator; two-digit suffices = undulator periodicity in mm. BM = bending magnet; SB = superbend; field strengths in Tesla.

whereby λ_m is the wavelength of the mth harmonic, λ_u is the periodicity of the undulator magnet array (typically measured in cm), the Lorentz factor $\gamma = \mathcal{E}/m_e c^2$ is the ratio of the electrons' storage-ring energy to their rest-mass energy (of the order of several thousand), and

$$K = 0.934\,\lambda_u[\mathrm{cm}]\,B_0[\mathrm{T}] \sim 1 \tag{11}$$

is the magnetic deflection parameter describing the ratio of the maximum angular excursion of the electron beam as it passes through the undulator's magnet array to the natural opening angle of the synchrotron radiation, which is itself equal to $1/\gamma$. The second term in the brackets, $\gamma^2\theta^2$, describes the contribution from off-axis radiation. This results in broad lobes on the low-energy flanks of the main undulator maxima.

Importantly, the ratio of the horizontal width of the electron beam to the amplitude of its oscillations induced by the undulator is, for third-generation facilities approximately 100. In contrast, this same ratio is approximately 10 or smaller for DLSRs. This means that the maximum off-axis angle for emitted undulator radiation at DLSRs is much smaller and hence this contribution is largely suppressed, as summarised in Figure 7.

This narrower electron beam presents several technological opportunities. Firstly, entire undulator maxima can be used for those experiments that do not require a very small relative bandwidth but require as many photons per unit time on the sample as is possible. At SLS 2.0, these might include certain types of diffraction techniques such as serial crystallography [9–13], lensless imaging that relies primarily on the transverse (and not longitudinal) coherence [14], and imaging techniques such as phase-contrast tomography [15, 16].

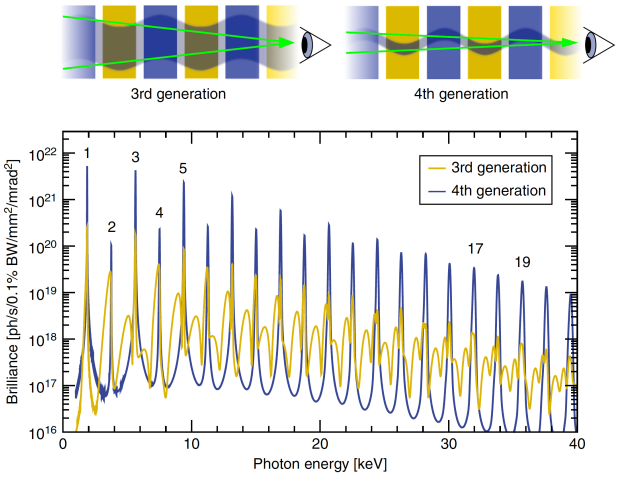

Figure 7. Comparison of the brilliance of undulator spectra at third- and fourth-generation facilities. Top: the width of the electron beam passing through an undulator at third-generation facilities is approximately two orders of magnitude larger than the oscillation amplitude, while at DLSRs, it might only be approximately ten times, or even less. Bottom: consequently, less off-axis radiation (given by Equation 10) is produced by undulators at DLSRs. Note also the enhanced brilliance at the spectral peaks for the DLSR. Both simulated spectra were generated for a U12 undulator (that is, $\lambda_u = 12$ mm) containing 120 magnet periods, for $K = 1.6$, 400 mA, and a storage-ring energy, currently used at SLS, of 2.4 GeV. Adapted from [8] with permission from John Wiley & Sons.

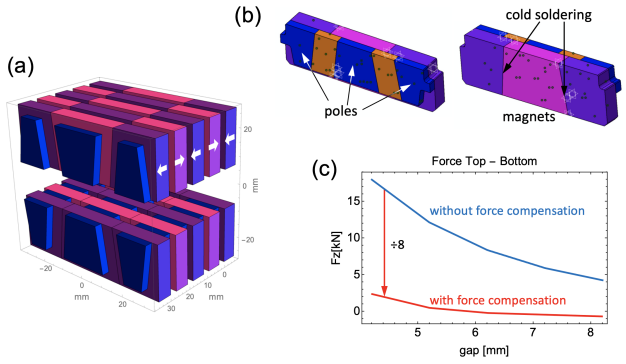

Figure 8. Novel developments in hard x-ray insertion devices. (a) The central Halbach array of poles and magnets can be made to be significantly narrower, thanks to the reduced lateral extent of the electron beam in the orbital plane as it passes through the ID in DLSRs compared to third-generation facilities. Consequently, the forces for a given central magnetic-field strength will be lower. Moreover, the central magnet array can be flanked by arrays in which the poles are opposed (N-N or S-S), thus reducing the total forces even more. The configuration is shown in (b). The reduction in force is typically a factor of eight or more (c), allowing for far more compact and inexpensive mechanical designs.

Secondly, the reduced oscillations of the electron beam due to the improved injection scheme from the booster means that as it passes along the undulator, the width of the magnets needed to produce a homogeneous field across the central axis can be reduced. This means that the forces acting on the undulator support structure become concomitantly smaller. Moreover, the additional space won by making the magnets narrower also allows the incorporation of two additional sets of magnets, one to each side of the central array, which, in contrast to the central array, are poled so that they repel (Figure 8). This will reduce the net forces on the undulator frame by well over an order of magnitude compared to standard devices used today, and will likely make them cheaper and much more compact and reliable.

A further ambitious R&D project in the area of hard x-ray insertion devices is being pursued as part of the upgrade program, namely the development of an ultra-short period hard x-ray device ($\lambda_u = 10$ mm) in order to access photon energies in excess of 50 keV, despite the moderate storage-ring energy of SLS 2.0 of 2.7 GeV. This requires high K-values in order to enhance the intensities of higher-harmonic radiation, which in turn means that magnetic-field strengths are required that can only be generated using superconducting materials (Equation 11) [17].

B. Soft x-ray undulators

DLSRs, with their smaller horizontal beam size, are more sensitive to vibrations arising from water cooling of the optical elements. The APPLE X undulators for SLS 2.0, with shorter period lengths, provide 50 % more periods, at higher magnetic-field strengths and increased electron energy. This increases the heat load on the front-end and into the beamlines by approximately a factor of five. Optical elements such as monochromators and mirrors at beamlines receiving radiation from these undulators require more aggressive cooling with potential vibration problems from the water flow.

The Knot-APPLE undulator configuration proposed in 2013 [18] and demonstrated in 2015 [19] will overcome this problem by shifting all the higher harmonics above the fundamental off the central axis, thus reducing the on-axis heat load. Following the earlier ‘figure-8’ concept for planar undulators at SPring-8, which guided higher harmonics away from the axis [20], the Knot scheme works for all polarisations in APPLE undulators. By adding an orthogonal magnetic field with three times longer period, the on-axis power can be reduced while maintaining a high degree of polarisation.

The horizontal field can be superimposed so that the APPLE concept with four magnet arrays can be kept. For SLS 2.0 APPLE X undulators, the Knot scheme will

be implemented based on a Halbach configuration with eight instead of four magnets per period. This gives about 5 % higher field and magnets of half thickness are anyhow needed. An optimisation study showed that even small orthogonal fields result in effective reductions (a factor 9 for a 90-mm and factor 4 for a 36-mm period) of the on-axis power with only a 5% reduction in the flux of the fundamental harmonic. A set of 24 magnets form a super-period using varying magnetization angles.

It should be noted that the Knot scheme is limited to the first harmonic. The photon energy of the Knot undulator depends on both fields and is therefore shifted towards lower energies. The new generation of synchrotrons will provide on-axis or close to on-axis injection schemes which enable the use the more effective APPLE X or APPLE 3 undulator configurations with a large K-value range so that the entire soft x-ray range from the carbon (ca. 280 eV) to the silicon K-edge (ca. 1850 eV) can be covered. However, there are two satellites around the fundamental which provide different polarisations but also of a high degree. They might be used to further extend the photon energy range.

IV. SLS 2.0 BEAMLINE PORTFOLIO AND SCIENCE PROGRAM

The future scientific mission of photon science at SLS will be founded firmly on already established fields of excellence at the Paul Scherrer Institute (PSI). Among others, the SLS to date has produced world-leading research in activities as varied as scanning lensless imaging (ptychographic tomography), single-wavelength diffraction of macromolecular molecules (native-SAD), full-field tomography, soft x-ray angular-resolved photoelectron spectroscopy (ARPES), and resonant inelastic x-ray scattering (RIXS). All of these techniques will profit considerably from the upgrade, which we summarise in this section.

A. Phase-contrast tomography

The overall flux increase and energy range extension of the new storage ring, coupled with a 5-T superbend at 'S-TOMCAT' and installation of a U10 undulator (briefly mentioned in Section III A) at 'I-TOMCAT', will lead to game-changing improvements for x-ray tomography at SLS 2.0 (See Figure 6). Moreover, the significantly larger horizontal transverse coherence length of SLS 2.0, given by the much-improved horizontal emittance, will yield an almost isotropic transverse coherence function. This translates to an enhanced image quality in phase-contrast images. S-TOMCAT, an upgrade of the present TOMCAT facility, will continue to accept larger samples up to the order of a centimeter linear dimension; The entirely new beamline I-TOMCAT will concentrate on samples that are typically of the order of 1 mm or smaller.

Phase-contrast imaging relies on the detection of interference fringes arising from subtle differential refraction of the x-ray beam at interfaces between materials with low absorption but slightly different refractive indices. Before the upgrade, the horizontal fringe visibility has been significantly reduced due to source size blurring. Much sharper fringes at SLS 2.0 will dramatically boost phase-contrast sensitivity. New phase-reconstruction algorithms that go beyond simple single-fringe detection are already under development in the community [21]. This will be particularly important for coarse-resolution scans in hierarchical multiscale imaging [22] and in high-energy experiments, both of which require larger propagation distances; and for high-speed measurements, where the enhanced fringe visibility will allow feature detection even for exposures with very poor signal-to-noise ratios [23]. Indeed, in fast tomography at SLS 2.0, it is expected that even for small samples with linear dimensions below 1 mm, the maximum data-acquisition rate, measured in several hundred tomograms per second, may no longer be limited by photon flux, but by the centripetal forces acting on the sample during rotation (with a synchrotron as the radiation source, we must rotate the sample rather than the source, in contrast to hospital CAT, where the patient is stationary and the source and detector rotate).

B. Ptychography and ptychographic tomography

In coherent diffraction imaging (CDI), coherent scattering patterns, also called 'speckle patterns', are used to computationally reconstruct 2D or 3D images, exceeding the resolving power of 'classical' x-ray microscope techniques, often by over two orders of magnitude. As in all scattering techniques, CDI needs to overcome the phase problem, that is, that the scattering intensities, rather than the amplitudes and phases, are recorded and thus the phase information is lost. In CDI and crystallography, order constraints such as positive electron density and interatomic distances, respectively, are employed to overcome the phase problem. In ptychography, an extended object is illuminated by coherent flux in a scanning mode, whereby there is significant overlap, of the order of 50 % or more, between successive illuminations (see Figure 9) [24, 25]. This not only provides the extremely strong constraint that the reconstructed real-space image of the overlap region of two illuminations must be consistent, but also affords the possibility of recording over volumes that are limited only by computing power/data storage; results composed of as many as tens of gigavoxels have already

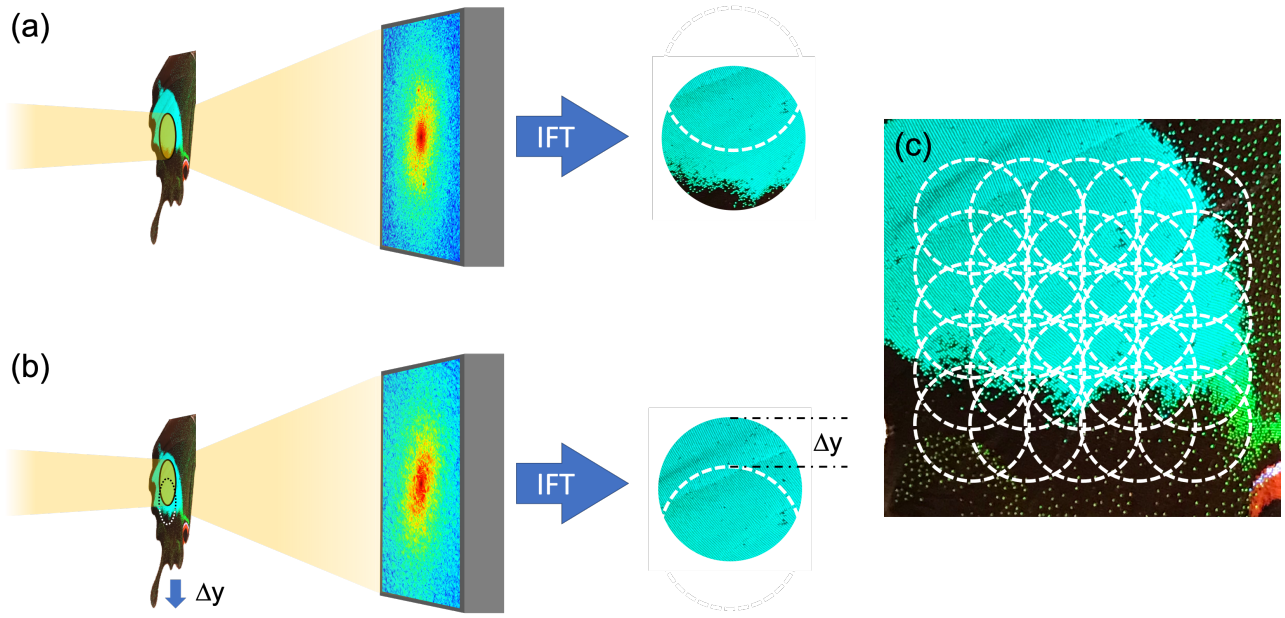

Figure 9. Principle of image reconstruction in ptychography. (a) An object is locally illuminated and the forward-scattered radiation is captured on an x-ray detector. If the phases of the individual amplitudes (these being proportional to the square root of the recorded intensity in each pixel) are correctly chosen, the inverse Fourier transform (IFT) will yield a real-space image of the region of the sample which was illuminated. (b) The sample is moved through a distance Δy which is smaller than the illumination diameter, and the next scattering pattern is recorded and IFT calculated. The region common to the first and second illuminations (i.e., the region encompassed by the dashed circle and the edge of the image) should thus be identical. It is this condition which is used to ensure that the phases have been correctly chosen, through an iterative algorithm [24]. (c) By scanning the sample over a large area and recording the scattering pattern at each step, very large volumes of the object can be reconstructed, limited only by the computer power and storage capacity on the one hand, and the dosage on the other.

been demonstrated.

Ptychography can thus be thought of as the marriage of CDI and scanning transmission x-ray microscopy (STXM).

The cSAXS beamline has been at the forefront of developments in ptychography and its application to the life [26] and engineering sciences [27], weak magnetic contrast [28–30], and sample dynamics [30]. Importantly, improvements in the upgraded beamline that extend well beyond the increase in coherent flux provided by the machine upgrade will mean that the available photon flux will be as much as three or four orders of magnitude greater than presently possible. These include an upgraded short-period undulator, a multilayer monochromator with a relative bandwidth of approximately 0.01, and high-efficiency reflective focussing optics to replace the diffractive optics used to date.

Advanced ptychography will not be limited to the cSAXS beamline. Both the PHOENIX and SIM beamlines have already begun programs in the tender and soft x-ray regimes, respectively, in close collaboration with cSAXS, notably with regards to the reconstruction algorithms. Emphasis will be laid on nano-spectroscopic methods on samples as diverse as vitrified biological specimens, nanomagnetic structures, and battery materials.

C. Macromolecular crystallography

Although, at the time of writing, well over 150'000 atomic-resolution structures of biological molecules and their complexes have been deposited in the Protein Data Bank (PDB), one important class of protein, namely membrane proteins, is extremely underrepresented; they constitute approximately 2 % of the deposited structures in the PDB, but account for one third of all known proteins and two thirds of medicinal drug targets. The primary reason for this anomaly is that membrane proteins and in particular their subset G-protein couple receptors (GPCRs), are, with some notable exceptions, extremely difficult to crystallize beyond the size of a few microns, due to their hydrophobic nature. This problem is mitigated to an extent by using lipidic cubic phases (LCPs) as the crystallization medium.

Nonetheless, MX studies of membrane proteins generally require micron or submicron focussing. At third-generation facilities, this demands an optical demagnification factor of the order of 100 or more with corresponding divergences on the sample of approximately 3 mrad. This can result in unacceptable blurring and overlapping of neighbouring diffraction peaks, especially for proteins exhibiting large unit cell dimensions. At fourth-generation facilities, this problem is reduced by an amount approximately equal to the improvement in emittance, namely a factor of fifty of thereabouts.

Only a limited amount of any given diffraction signal can be obtained from a given crystal before radiation damage sets in. Individual microcrystals normally suffer too much radiation damage before they can deliver a complete data set for structure determination, hence diffraction data from multiple crystals are merged. Prompted by successes in serial femtosecond crystallography pioneered at XFELs, there has been a concerted effort towards similar approaches using synchrotron radiation in a technique coined synchrotron serial crystallography (SSX) [13]. SSX can be carried out at both room temperature and cryogenic conditions, requiring novel techniques in sample preparation, delivery, data collection, and processing. Indeed, room-temperature crystallography is experiencing a renaissance through SSX [11]. Despite the one to two orders of magnitude reduction in the highest tolerable dose compared to cryo-MX, RT-SSX offers several advantages, including sampling conformational landscapes, dispensing with cryoprotectants, and, complementary to fs – ns studies at XFELs, providing the possibility of investigating dynamic processes down to microsecond time scales. It is noted that, in the era of COVID-19, MX and cryoEM have proven to be highly effective complementary tools in understanding the structural nature and biochemical pathways of this novel virus, leading to an unprecedented program of rapid drug discovery and vaccine development [31].

Most membrane proteins are relatively small – for example, GPCRs are almost all under 40 kDa, excluding them from investigation using cryo-EM. Even molecules up to 250 kDa cannot, in almost all cases, be investigated via cryo-EM with a resolution that is sufficient for atomic-scale studies. MX at SLS 2.0 will therefore concentrate on such systems, individually tailoring case-for-case the division of the improved emittance between divergence and focus size.

SSX will function far more efficiently and allow a whole vista of new macromolecules to be investigated with the micron- and submicron-sized parallel beams promised by SLS 2.0. Since many membrane proteins are expected to be novel, experimental phasing will be required to reveal their structures. Recent progress in native-SAD phasing (in which the PSI is a leading player) has led to great advances in *de novo* phase determination [32]. SLS 2.0 will provide a timely opportunity to optimize the existing three MX beamlines for native-SAD experiments, which require x-rays down to as low as 3 keV and sample environments with minimum background scattering and absorption.

Higher photon intensities than are generally accessible for the present MX beamlines at SLS are possible by increasing the relative bandwidth of the incident monochromatized radiation. Except for the very largest-unit-cell samples, an increase in bandwidth, and hence also photon-delivery rates, by a factor of 10 through the use of multilayer monochromators, could be easily tolerated. Combined with detectors capable of frame-rates of hundreds of Hz, SSX at SLS 2.0 will not only enable biologists to study structure and function of largely unexplored protein families, but also pave the way for high-throughput, structure-based, drug discovery of membrane proteins ('fragment screening'), an application entirely unsuited to cryo-EM, but one that will become still more central to MX as the realm of membrane proteins and GPCRs begins to reveal itself.

V. CONCLUDING REMARKS

Electron-accelerator photon sources have a remarkable track record in science, technology and biomedicine. The underlying physics as well as a demand for seeing matter at the atomic and nanoscale ensure that they will continue to be essential for scientific and technical progress in the future. Therefore, most third-generation electron storage rings are either considering or actively undergoing an upgrade to a DLSR. At the Paul Scherrer Institute, the plans for the upgraded SLS 2.0 extend beyond simple improvements of the emittance (and thereby also the brilliance), including novel magnet-lattice elements and x-ray sources pioneered at the PSI. This will maintain the pre-eminence of PSI, the ETH Domain, and Switzerland in photon science, which has been established by the current SLS and SwissFEL for the foreseeable future.

The machine upgrade in conjunction with novel source technologies will increase the most relevant experimental parameters at the endstations by well over two orders of magnitude in the hard x-ray regime (10), which will have very substantial benefits to many methods, including ptychography, full-field tomography, macromolecular crystallography, soft x-ray ARPES, and resonant inelastic x-ray scattering.

Indeed, even greater improvements by up to another factor of 100 are anticipated through adaptations in x-ray optics, most notably in the use of multilayer monochromators in stead of crystal monochromators at hard x-ray beamlines, and the substitution of hitherto more conventional but lossy refractive and diffractive focussing elements such as compound refractive lenses

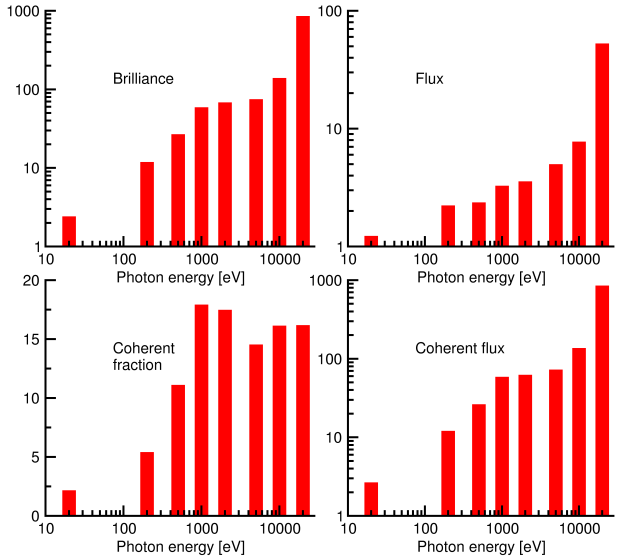

Figure 10. Improvement factors in brilliance, flux, coherent fraction, and coherent flux for the SLS 2.0 upgrade compared to the present SLS, with the new storage-ring energy of 2.7 GeV, for selected photon energies. The undulators assumed in the original SLS are UE212 (8.4 m) for 20 and 200 eV, UE56 (3.6 m) for 500, 1000, and 2000 eV, and U19 (1.8 m) for higher photon energies. The corresponding undulators in SLS 2.0 are UE90 (4.4 m), UE36 (4.4 m), and CPMU15 (3 m).

and Fresnel zone plates with reflecting elements such as Kirkpatrick-Baez mirrors, which can be made to be more compact than previously possible, thanks to the reduced source sizes.

The design, construction and exploitation of SLS 2.0 will enable not only advanced research and education, but also the continued excellence of technology transfer demonstrated by SLS these last two decades, especially in partnership with InnovAare, the node of the Swiss Innovation Park to be located next to SLS 2.0.

SLS 2.0 is highly synergistic with SwissFEL, co-located at PSI to create a unique centre for accelerator-based photon science in Switzerland. The people and expertise which enabled the recent completion of SwissFEL are now deployed for SLS 2.0. Many of the technologies developed for the SwissFEL project, ranging from serial crystallography to Apple-X undulators, were originally developed for SwissFEL and our now being exported to SLS 2.0; we expect similar fertilization of the Porthos upgrade of SwissFEL which will follow SLS 2.0.

ACKNOWLEDGEMENTS

Many thanks go to all the many contributors to the SLS 2.0 project, from the accelerator department, through support and logistics, IT, to the many beamline staff, not least Andreas Menzel, Marco Stampanoni, and Meitian Wang.

[1] M. Selmer, C. M. Dunham, F. V. Murphy IV, A. Weixlbaumer, S. Petry, A. C. Kelley, J. R. Weir, and V. Ramakrishnan. Structure of the 70S ribosome complexed with mRNA and tRNA. *Science*, 313:1935, 2006.

[2] A. Weixlbaumer, H. Jin, C. Neubauer, R. M. Voorhees, S. Petry, A. C. Kelley, and V. Ramakrishnan. Insights into translational termination from the structure of RF2 bound to the ribosome. *Science*, 322:953–956, 2008.

[3] R. M. Voorhees, A. Weixlbaumer, D. Loakes, A. C. Kelley, and V. Ramakrishnan. Insights into substrate stabilization from snapshots of the peptidyl transferase center of the intact 70S ribosome. *Nat. Struct. Mol. Biol.*, 16:528–533, 2009.

[4] M. Jinek, F. Jiang, D. W. Taylor, S. H. Sternberg, E. Kaya, E. Ma, C. Anders, M. Hauer, K. Zhou, S. Lin, M. Kaplan, A. T. Iavarone, E. Charpentier, E. Nogales, and J. A. Doudna. Structures of Cas9 endonucleases reveal RNA-mediated conformational activation. *Science*, 343:1247997, 2014.

[5] W. Joho, P. Marchand, L. Rivkin, and A. Streun. Design of a Swiss Light Source (SLS). In *Proceedings of the 4th European Particle Accelerator Conference (EPAC1994)*, Proceedings of the European Particle Accelerator Conference, pages 627–629, Singapore, 1994. World Scientific.

[6] J. Bengtsson, W. Joho, P. Marchand, L. Rivkin, and A. Streun. Status of the Swiss Light Source Project SLS. In *Proceedings of the 5th European Particle Accelerator Conference (EPAC1996)*, Proceedings of the European Particle Accelerator Conference, pages 685–687, London, UK, 1996. Institute of Physics.

[7] M. Eriksson, L. J. Lindgren, M. Sjostrom, E. Wallen, L. Rivkin, and A. Streun. Some small-emittance light-source lattices with multi-bend achromats. *Nucl. Instrum. Methods A*, 587:221, 2008.

[8] P. R. Willmott. *Introduction to Synchrotron Radiation – Techniques and Applications*. John Wiley and Sons, 2nd edition, 2019.

[9] S. Botha, K. Nass, T. R. M. Barends, W. Kabsch, B. Latz, F. Dworkowski, L. Foucar, E. Panepucci, M. Wang, R. L. Shoeman, I. Schlichting, and R. B. Doak. Room-temperature serial crystallography at synchrotron x-ray sources using slowly flowing free-standing high-viscosity microstreams. *Acta Crystallogr. D*, 71:387–397, 2015.

[10] P. Nogly, D. James, D. Wang, T. A. White, N. Zatsepin, A. Shilova, G. Nelson, H. Liu, L. Johansson, M. Heymann, K. Jaeger, M. Metz, C. Wickstrand, W. Wu,

P. Bath, P. Berntsen, D. Oberthuer, V. Panneels, V. Cherezov, H. Chapman, G. Schertler, R. Neutze, J. Spence, I. Moraes, M. Burghammer, J. Standfuss, and U. Weierstall. Lipidic cubic phase serial millisecond crystallography using synchrotron radiation. *IUCrJ*, 2:168–176, 2015.

[11] F. Stellato, D. Oberthür, M. Liang, R. Bean, C. Gati, O. Yefanov, A. Barty, A. Burkhardt, P. Fischer, L. Galli, R. A. Kirian, J. Meyer, S. Panneerselvam, C. H. Yoon, F. Chervinskii, E. Speller, T. A. White, C. Betzel, A. Meents, and H. N. Chapman. Room-temperature macromolecular serial crystallography using synchrotron radiation. *IUCrJ*, 1:204–212, 2014.

[12] C. Gati, G. Bourenkov, M. Klinge, D. Rehders, F. Stellato, D. Oberthür, O. Yefanov, B. P. Sommer, S. Mogk, M. Duszenko, C. Betzel, T. R. Schneider, H. N. Chapman, and L. Redecke. Serial crystallography on in vivo grown microcrystals using synchrotron radiation. *IUCrJ*, 1:87–94, 2014.

[13] K. Diederichs and M. Wang. Serial synchrotron x-ray crystallography (SSX). *Methods Mol. Biol.*, 1607:239–272, 2017.

[14] F. Pfeiffer. X-ray ptychography. *Nature Photonics.*, 12:9–17, 2018.

[15] T. J. Davis, D. Gao, T. E. Gureyev, A. W. Stevenson, and S. W. Wilkins. Phase-contrast imaging of weakly absorbing materials using hard x-rays. *Nature*, 373:595–598, 1995.

[16] A. Momose, T. Takeda, Y. Itai, and K. Hirano. Phase-contrast x-ray computed tomography for observing biological soft tissues. *Nature Med.*, 2:473–475, 1996.

[17] M. Calvi, M. D. Ainslie, A. Dennis, J. H. Durrell, S. Hellmann, C. Kittel, D. A. Moseley, T. Schmidt, Y. Shi, , and K. Zhang. A GdBCO bulk staggered array undulator. *Supercond. Sci. Technol.*, 33:014004, 2020.

[18] S. Sasaki, A. Miyamoto, and S. Qiao. Design study of KNOT-APPLE undulator for PES-Beamline at SSRF. *Proc. PAC2013*, pages 1043–1054, 2013.

[19] F. Ji, R. Chang, Q. Zhou, W. Zhang, M. Ye, S. Sasaki, and S. Qiao. Design and performance of the APPLE-Knot undulator. *J. Synchrotron Rad.*, 22:901–907, 2015.

[20] T. Tanaka and H. Kitamura. Analysis of figure-8-undulator radiation. *J. Synchrotron Rad.*, 3:47–52, 1996.

[21] J. Villanova, R. Daudin, P. Lhuissier, D. Jauffres, S. Y. Lou, C. L. Martin, S. Laboure, R. Tucoulou, G. Martinez-Criado, and L. Salvo. Fast in situ 3D nanoimaging: a new tool for dynamic characterization in materials science. *Materials Today*, 20:354–359, 2017.

[22] H. Dejea, P. Garcia-Canadilla, A. C. Cook, E. Guasch, M. Zamora, F. Crispi, M. Stampanoni, B Bijnens, and A. Bonnin. Comprehensive analysis of animal models of cardiovascular disease using multiscale x-ray phase contrast tomography. *Sci. Reports*, 9:6996, 2019.

[23] F. García-Moreno, P. H. Kamm, T. R. Neu, F. Bülk, R. Mokso, C. M. Schlepütz, M. Stampanoni, and J. Banhart. Using x-ray tomoscopy to explore the dynamics of foaming metal. *Nature Commun.*, 10:3762, 2019.

[24] P. Thibault, M. Dierolf, A. Menzel, O. Bunk, C. David, and F. Pfeiffer. High-resolution scanning x-ray diffraction microscopy. *Science*, 321:379–382, 2008.

[25] M. Guizar-Sicairos and P. Thibault. Ptychography: A solution to the phase problem. *Physics Today*, 74:42–48, 2021.

[26] S. H. Shahmoradian, E. H. R. Tsai, A. Diaz, M. Guizar-Sicairos, J. Raabe, L. Spycher, M. Britschgi, A. Ruf, H. Stahlberg, and M. Holler. Three-dimensional imaging of biological tissue by cryo x-ray ptychography. *Sci. Rep.*, 7:6291, 2017.

[27] M. Holler, M. Guizar-Sicairos, E. H. R. Tsai, R. Dinapoli, E. Müller, O. Bunk, J. Raabe, and G. Aeppli. High-resolution non-destructive three-dimensional imaging of integrated circuits. *Nature*, 543:402–406, 2017.

[28] C. Donnelly, V. Scagnoli, M. Guizar-Sicairos, M. Holler, F. Wilhelm, F. Guillou, A. Rogalev, C. Detlefs, A. Menzel, J. Raabe, and L. J. Heyderman. High-resolution hard x-ray magnetic imaging with dichroic ptychography. *Phys. Rev. B*, 94:064421, 2016.

[29] C. Donnelly, M. Guizar-Sicairos, V. Scagnoli, S. Gliga, M. Holler, J. Raabe, and L. J. Heyderman. Three-dimensional magnetization structures revealed with x-ray vector nanotomography. *Nature*, 547:328–331, 2017.

[30] C. Donnelly, K. L. Metlov, V. Scagnoli, M. Guizar-Sicairos, M. Holler, N. S. Bingham, J. Raabe, L. J. Heyderman, N. R. Cooper, and S. Gliga. Experimental observation of vortex rings in a bulk magnet. *Nat. Phys.*, 17:316–321, 2021.

[31] M. L. Lynch, E. H. Snell, and S. E. J. Bowman. Structural biology in the time of COVID-19: perspectives on methods and milestones. *IUCrJ*, 8:335–341, 2021.

[32] T. Weinert, V. Olieric, S. Waltersperger, E. Panepucci, L. Chen, H. Zhang, D. Zhou, J. Rose, A. Ebihara, S. Kuramitsu, D. Li, N. Howe, G. Schnapp, A. Pautsch, K. Bargsten, A. E. Prota, P. Surana, J. Kottur, D. T Nair, F. Basilico, V. Cecatiello, S. Pasqualato, A. Boland, O. Weichenrieder, B.-C. Wang, M. O. Steinmetz, M. Caffrey, and M. Wang. Fast native-SAD phasing for routine macromolecular structure determination. *Nat. Methods*, 12:131–133, 2015.